A. Donizetti, T. Bellosta, A. Guardone
*Ice Shape Convergence in Multi-Step Ice Accretion Simulations over Straight Wings*
in: AIAA Scitech 2024 Forum, AIAA, 2024, ISBN: 9781624107115, p. 1-19, AIAA 2024-2679
[AIAA Scitech 2024 Forum, Orlando, FL, USA, 8-12 Jan. 2024]
doi:10.2514/6.2024-2679

# Ice Shape Convergence in Multi-Step Ice Accretion Simulations over Straight Wings

Donizetti A.*, Bellosta T. †, Guardone A. ‡,
*Politecnico di Milano, Milano, Italy, 20154*

**Local errors in the geometrical description of the ice front are amplified in multi-step simulations over conformal meshes due to the coupling of aerodynamics, water impingement, ice accretion, and grid deformation. Small perturbations in the initial phase of ice formation possibly result in dramatically different ice shapes which can hinder the stability of the multi-step procedure. This problem is analyzed by investigating the combined effects of space and time discretization on the ice growth over airfoils and three-dimensional wings. We propose an automatic procedure for selecting the time interval for the update of the aerodynamics and particle impingement. A local growth limiter $\lambda$ is introduced here to bound the local ice thickness growth to be comparable to the local grid spacing on the surface, resulting in an automatic adaptive time-step to be used in the multi-step simulation. Examples are provided for three-dimensional cases under both rime and glaze conditions over straight wings. These examples highlight the different accretion mechanisms of the two ice regimes and preliminary indicate that ice-shape convergence can be achieved for low values of $\lambda$.**

## I. Introduction

In aeronautical applications, ice formation during flight poses a significant threat, adversely impacting the aircraft's aerodynamics. To gain a deeper understanding of how ice accumulation affects aerodynamic performance and to design efficient ice protection systems, numerical simulations and ice accretion tools [1–5] have gained increasing importance in the last few years. These tools allow for the simulation of diverse and potentially extreme conditions that complement experimental and in-flight studies, possibly saving significant costs in the aircraft design and icing certification processes [6].

In-flight icing is a complex problem that involves various disciplines, including aerodynamics, multi-phase flows, thermodynamics, and meshing capabilities. As ice progressively forms on the aircraft, it alters the surrounding flow field, influencing the trajectories of cloud droplets and, ultimately, the ice shape. A multi-step—known as multi-shot—approach can be implemented to consider this feedback effect and achieve accurate ice shape predictions[7]. The multi-step concept stems from the existence of two separate time scales: the aerodynamic one and the ice accretion one. The former is proportional to the flow speed divided by a suitable characteristic length, e.g. the chord of the profile. The latter governs the growth of ice and the associated phase-change problem. Given that the time scale of ice accretion is significantly larger than that of aerodynamics and droplet fields, it is possible to compute the rate of ice accumulation by solving the heat and mass balance on the surfaces while maintaining a constant aerodynamic solution, namely, geometrical shape. Under this quasi-steady assumption, the total icing exposure time is divided into smaller time steps. The aerodynamic flow field, the amount and distribution of the cloud water droplets impinging on the selected surfaces, and the ice growth rate are computed in sequence at each step. At the end of each time step, the new geometry and the corresponding surrounding computational mesh must be updated in response to the ice growth. This operation is usually the most critical phase of the multi-step loop, especially if a fully automated procedure is desired.

A critical issue of multi-step methods is the coupling between geometry variation and collection efficiency. Geometry perturbations of the surface (iced) geometry result in a non-uniform distribution of the collection efficiency exhibiting multiple local peaks, ultimately leading to additional perturbations of the iced surface. As shown in Fig. 1a, this results in an auto-amplifying phenomenon [8, 9], which can hinder the stability of the multi-step procedure or lead to non-physical ice shape predictions.

The ambient conditions in the considered example result in the formation of so-called rime ice. Due to the extremely low temperatures, all incoming water mass freezes upon impingement. Ten sequential accretion steps are performed,

*PhD Student, Department of Aerospace Science and Technology, alessandro.donizetti@polimi.it
†Assistant Professor, Department of Aerospace Science and Technology, tommaso.bellosta@polimi.it
‡Full Professor, Department of Aerospace Science and Technology, alberto.guardone@polimi.it

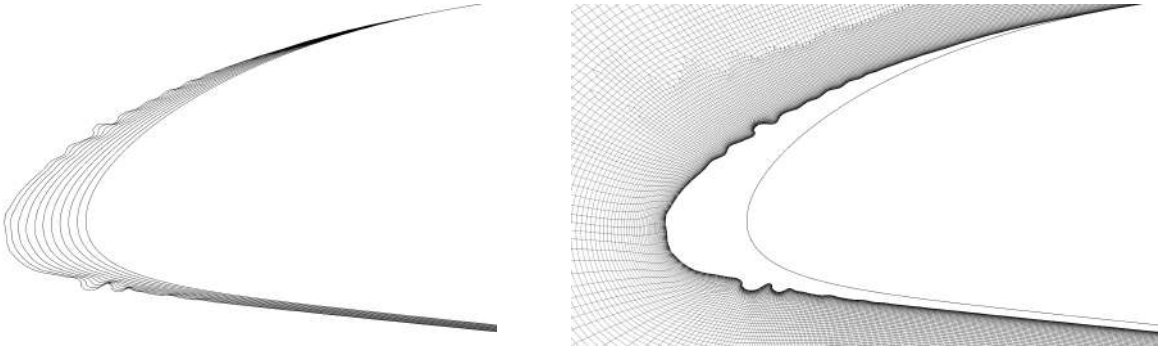

**(a) 10 steps evolution of a rime ice shape.** **(b) Final volume mesh.**

**Fig. 1 Multi-step simulation over a NACA 23012 airfoil obtained with a mesh deformation approach for the geometry update. Ice shape oscillations develop on the suction and pressure side of the airfoil.**

with a total exposure time of 300 seconds. Concerning spatial discretization, the iced region is characterized by an initial uniform distribution of $h_{grid}/c = 5 \cdot 10^{-4}$, where $c$ is the airfoil chord. Then, given the simplicity of the considered test case and to avoid any interpolation error related to the remeshing process, the grids for the following time steps are obtained with a grid deformation approach [10].

This simple example highlights several crucial problems for multi-step simulations of in-flight ice accretion. The first concerns the choice of the duration of the various time steps, especially when no experimental data is available, and preliminary guesses about the ice shape must heavily rely on the user's experience. The second one regards the formation of the oscillations mentioned above and the importance of highly robust methods based, for instance, on remeshing techiniques [11, 12], level-set methods [13, 14], or immersed boundary methods [15, 16] capable of overcoming mesh entanglement and grid intersections, which typically occur with standard deformation techniques when dealing with these complex ice shapes. Remeshing is also unavoidable to preserve the mesh quality even if no grid intersections occur. Indeed, as ice accumulates over the surface, the mesh density begins to coarsen because the number of nodes remains unchanged in the deformation process but they are spread over a larger surface area, as seen in Fig. 1b, where, in the leading edge stagnation area, the local grid spacing has become five times larger than the initial one. Finally, considering in addition the cascade effects in multi-step simulations, assessing the ice shape convergence of a multi-step simulation effectively is an open challenge.

This work aims to investigate the combined effects of space and time discretization on the ice growth on airfoils and suggests a simple, automatic technique for time-step selection based on a local growth limiter $\lambda$ to bound the local ice thickness growth. The parameter $\lambda$ relates the local grid spacing in the tangential direction to the ice thickness, namely, $h_{ice} = \lambda h_{grid}$. Most of the icing tools compute the ice thickness on the generic element from the corresponding ice growth rate per unit area $\dot{m}_{ice}$ as:

$$h_{ice} = \frac{\dot{m}_{ice}}{\rho_{ice}} \Delta t \tag{1}$$

where $\rho_{ice}$ is the ice density. The combination of the above equations leads to a simple and automatic definition of the duration of each step of the multi-step simulation:

$$\Delta t = \lambda \min \left( \frac{h_{grid}}{\dot{m}_{ice}/\rho_{ice}} \right) \tag{2}$$

Note that independently from the parameter $\lambda$ and the grid ice spacing $h_{grid}$, which may be kept constant throughout the simulation, the duration of each inner step may change depending on the computed growth rate, which is determined by the current collection efficiency and by the mass and energy conservation equations. This work analyses different spatial and temporal, i.e. $\lambda$, discretization to assess their impact on the predicted ice shape. It is organized as follows. The PoliMIce ice accretion software is first briefly introduced in the methodology section II, focusing on how ice shape instabilities would cause mesh intersection in standard mesh deformation methods and how those are treated with the level-set-based method implemented in PoliMIce. Section III includes numerical simulations of test cases selected from the $1^{st}$ Ice Prediction Workshop (IPW) [17] both in rime and glaze conditions. Final comments and future developments of the proposed methodology are given in section IV.

## II. Methodology

The main building blocks of a multi-step ice accretion simulation are the computation of the aerodynamic flow field, of the amount and distribution of the cloud water droplets impinging on the selected surfaces, of the ice growth rate, and the updating of the geometry and corresponding surrounding mesh. The following sections describe these four steps in more detail, focusing on the novel strategy proposed for the implicit representation of the iced boundary and the automatic remeshing procedure required to generate the new CFD grid.

### A. Aerodynamic solver

Aerodynamic simulations of the external airflow are performed here using SU2 [18]. A node-centered finite volume method (FVM) is applied on arbitrary unstructured meshes using a standard edge-based data structure on a dual grid with median-dual control volumes. Convective fluxes are discretized at each edge midpoint using an upwind scheme. Discretization using Roe's approximate Riemann solver [19] is coupled with a linear reconstruction via the MUSCL approach to yield a second-order scheme in space. Viscous fluxes are discretized using a corrected average of gradients approach. Source terms are approximated at each node using a piecewise constant reconstruction within each control volume. Gradients are obtained via a weighted least-squares approach. The aerodynamic field is computed as a solution to the Reynolds-averaged Navier-Stokes (RANS) equations, which is used in this study in tandem with the Spalart–Allmaras (SA) [20] turbulence model. The system's solution is obtained implicitly using a defect-correction approach with pseudo-time continuation. The mean flow and turbulence systems are solved sequentially with the flexible minimal residual method, and the ILU(0) factorization of the approximate jacobian is used as a preconditioner. A local value of the time step coupled with an adaptive ramping strategy for the CFL is used to accelerate the convergence of the steady-state solution [21].

### B. Particle tracking module

The droplet solver computes the collection efficiency $\beta$ over the aircraft, which is proportional to the water mass collected at a given location on the surface. It requires the computation of the two-phase flow of water and air. Due to the scales at play in ice accretion and, in particular, the concentration of water droplets, their effects on the solution of the airflow field can usually be neglected so that the computation of the aerodynamics can be performed independently of the water droplets. This assumption leads to the so-called one-way coupled approach; only the airflow field can affect the motion of water droplets. The in-house particle tracking code is based on a Lagrangian framework, and it is used to simulate clouds containing supercooled water droplets [22, 23]. The Lagrangian framework allows straightforward modeling of supercooled water droplets' effects, such as splashing, aerodynamic breakup, and deformation, and can deal with secondary particles.

The cloud impinging the aircraft surfaces is represented as a single front initially placed at an arbitrary distance ahead of the aircraft. This distance is set so droplets are traced starting from an unperturbed region of the domain. As the final result depends on the particle resolution, a strategy was developed to automatically refine the seeding region by adding new particles where needed. The seeding front, initially uniform, is discretized as a structured mesh of linear (in 2D) or quadrilateral (in 3D) elements. Elements are incrementally split at each iteration, evolving the current cloud front and computing the collection efficiency $\beta$ on the surface. The simulation stops when the difference in the $L_2$ norm between two consecutive collection efficiency calculations is below a user-supplied threshold. In the present work, the chosen threshold is $1 \cdot 10^{-6}$. In practical applications, clouds are poly-dispersed. A standard approach deals with this problem by tracking a uniform cloud of droplets with a diameter equal to the Median Volume Diameter (MVD). This is the median value of the particle diameter of the entire cloud. Half the mass comes from droplets of a diameter smaller than the cloud MVD, and half from particles larger than the MVD. A more refined discretization of the particle size distribution can be considered by subdividing the droplets' size probability distribution function in a given number of so-called bins. A simulation can be performed for each bin, and the final collection efficiency can be obtained as a weighted sum of the bins' $\beta$. In this work, unless otherwise specified, the droplets' size distribution is divided into seven bins, of which three are smaller and three are larger than the MVD. The relative percentage is set according to the wind tunnel data. This is usually a good compromise between computational effort and the accuracy of the solution, in particular concerning the impinging limits, which are determined by the larger droplets.

### C. Ice accretion module

The in-house code PoliMIce [24] is used for computing the ice accretion. Computing the thickness of the forming ice layer amounts to solving a phase change problem over the body surface. Typically, surfaces are first discretized in computational cells, and a one-dimensional Stefan problem [25] is solved for each control volume. Early icing tools rely on the approximate solution of the Stefan problem proposed by Messinger in 1953 [26] for aeronautical applications. The model reported in [27] embeds Messinger's mass and energy balance in an iterative loop to determine the mass inflow and outflow between elements. It allows the model to be suitable for complex 3D geometries, and it is widely used in modern ice prediction tools, as is the PDE formulation of [28]. In 2001 Myers [29] proposed an improved version of Messinger's model, accounting for the temperature profile in the ice layer. A further modification to Myers' model, based on the exact local solution of the unsteady Stefan problem, is implemented in PoliMIce [30]. It includes models for mass fluxes related to sublimation, allows mass transfer from rime to glaze cells, and introduces a new temperature profile, different from the linear one proposed by Myers to be consistent with the hypothesis of constant wall temperature. The surface roughness is estimated a-priori with the empirical formula of Shin [31], as a function of liquid water content (LWC), static air temperature, and freestream velocity. It provides an equivalent sand-grain roughness, $k_s$, which is needed by the Boeing extension for the SA turbulence model[32]. In this work, the heat transfer coefficient is computed by employing two simulations of the flow field with two different boundary conditions for the wall temperatures. Note that the ice accretion problem is assumed to be zero-dimensional and that a piecewise constant representation of the solution is obtained over each cell. In the multi-step procedure, the water film distribution and all the icing data are interpolated from the previous step through a nearest-neighbor search algorithm.

### D. Geometry updating module

In a multi-step ice accretion simulation, updating the geometry is often the most challenging task, especially when simulating complex ice shapes. In fact, this process must be robust and automated so that no user intervention is required throughout the process. Following the work proposed in [14], the new ice-air interface is represented as the zero-contour level of a level-set function[33]. Given a 2D, or 3D, domain $\Omega \subset \mathbb{R}^{2,3}$, a curve, or a surface, can be represented by a certain level-set (or isocontour) of the auxiliary function $\phi(\mathbf{x})$, with $\mathbf{x} \in \Omega$. Considering the accretion of ice over the boundary of the computational domain otherwise empty, $\phi(\mathbf{x})$ is an implicit function defined so that:

- $\phi(\mathbf{x}, t) < 0$ in the portion of the domain occupied by material,
- $\phi(\mathbf{x}, t) > 0$ in the portion of the domain not occupied by material,
- $\phi(\mathbf{x}, t) = 0$ at the interface.

In [14], the discrete level-set field was built considering the ice thickness to be accreted at the airfoil boundary and the distance of each grid node from it. This work defines the level-set scalar field with a novel algorithm, which can accurately describe the new ice-air interface even for large displacements. The procedure can be briefly summarized as follows:

1) Starting from the Lagrangian deformation of the iced surface, a triangular volume mesh, or tetrahedral mesh in the 3D case, is built according to the computed ice thickness distribution.
2) Employing a nearest neighbor search algorithm with a kd-tree structure[34], each volume point is assigned a value of $\phi$ of either +1 or -1, depending if it lies outside (+1) or within (-1) the deformed simplicial iced mesh.
3) To increase the accuracy of the reconstructed ice-air interface, the distance from the closest, Lagrangian-like deformed boundary is computed for each node. In this way, the ice-air interface is described continuously in the volume field and not only by means of constant values, and large displacements can be robustly reconstructed through the level-set function, which was not ensured with the distance method due to the absence of directional information when computing the distance values.

Once the nodal values for the level set function $\phi(\mathbf{x})$ are defined over the discrete domain $\Omega_h$, one needs to extract the zero level curve of $\phi(\mathbf{x})$. The implicit domain meshing implemented in the open-source library Mmg [35] was used to accomplish this task. It can be summarized in the following three steps:

1) Each simplex element intersected by the zero level curve of the level-set function $\phi$ is marked, considering the relative signs of $\phi$ at the nodes of the grid element.
2) For each element, the edges intersected by the level-set are identified, and a new point is inserted along each edge in the correspondence of the zero level curve. To locate the new point, a linear interpolation is performed between the values at the nodes delimiting the edge.
3) Finally, local mesh refinement is performed, swapping edges and inserting, removing, and relocating mesh vertices to improve the overall mesh quality.

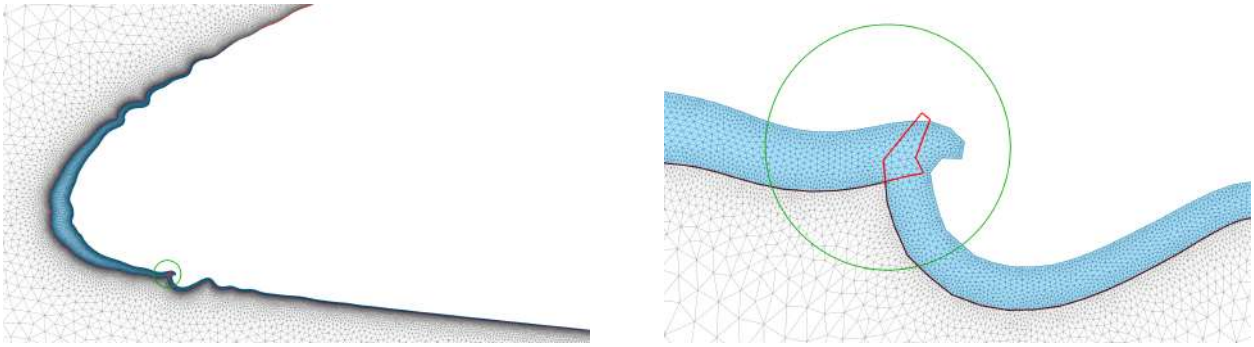

**(a) Discrete definition of the level-set function over the simplicial computation domain. The blue elements are characterized by $\phi < 0$, the white ones by $\phi > 0$, and the red curve represents the ice-air interface as the zero-contour level of $\phi$.**

**(b) Zoom on a mesh entanglement in the lower side given by a lagrangian deformation of the surface nodes, represented in red. The actual geometry retrieved through the proposed strategy is represented in black.**

**Fig. 2 Schematic representation of the implicit domain strategy adopted for the representation of the ice-air interface, represented in red, during a generic step of a multi-step simulation, and avoidance of mesh entanglement during the geometry update.**

The reader is referred to [35] for the implementation details.

Fig. 2 represents a typical output of the depicted implicit domain strategy. In particular, the portion of the domain occupied by ice is represented in blue, the portion occupied by air is represented in white, and the red line constitutes the air-ice interface target. A similar result could also be obtained with a ray tracing algorithm, employing only the deformed surface. However, the distinction between inside and outside points would be wrongly computed if mesh entanglements occur. With the proposed algorithm instead, in case of overlap between the deformed elements, the generic volume point defining the level-set function $\phi$ would be inside two, or more, elements, still providing the correct sign of $\phi$.

One can extract separately each portion of the domain (for instance, in ice accretion problems, the part of the mesh with negative $\phi$ can be used to investigate heat transfer properties or ice cracking patterns for shedding [36]), as well as the set of edges connecting all points at $\phi = 0$ which represents the target ice-air interface at the new time step.

In the context of a multi-step procedure, when dealing with the 2D scenario, the selected points undergo a sequential reordering, e.g., starting from the trailing edge in a counterclockwise direction, and given as input to the mesh generator Pointwise [37]. For three-dimensional geometries, the remeshing procedure described in [38] is used. After the level-set function is computed, the interface elements are extracted along with the remaining clean body elements. The new interface elements are usually ill-shaped since they result from the splitting of the volume tetrahedra. Yet, interface elements provide a conformal surface discretization of the ice-air interface. Finally, he ice-air interface is remeshed using isotropic elements to obtain a body-fitted surface mesh with good-quality elements without changing the clean body elements.

Depending on the chosen aerodynamic solver, either structured, unstructured, or hybrid meshes can be generated. In this study, the aerodynamic flow field is computed using the Navier-Stokes solver of the open-source CFD solver SU2 [18]. Hybrid body-fitted meshes are generated with Pointwise starting from the interface-compliant boundary discretization. These meshes are designed to meet the requirements of $y+ < 1$ for the first layer, as required by the Spalart-Allmaras turbulence model [20] employed in this work. Note that the mesh generated for the next CFD computations is not necessarily related to the one adopted for defining the level-set function $\phi$ in the implicit domain meshing strategy of Mmg.

## III. Results

This section presents an analysis of the effect of spatial and temporal discretization on the final ice shape, both for rime and glaze ice shapes over straight wings. The first two test cases considered are 2D cases, i.e., icing over a straight wing, namely Case-241 and Case-242 from the $1^{st}$ AIAA Ice Prediction Workshop (IPW) [17]. In both cases, the airfoil is an 18-inches NACA 23012. Test conditions are reported in Table 1. For each case, four different $\lambda$ values, namely 5,

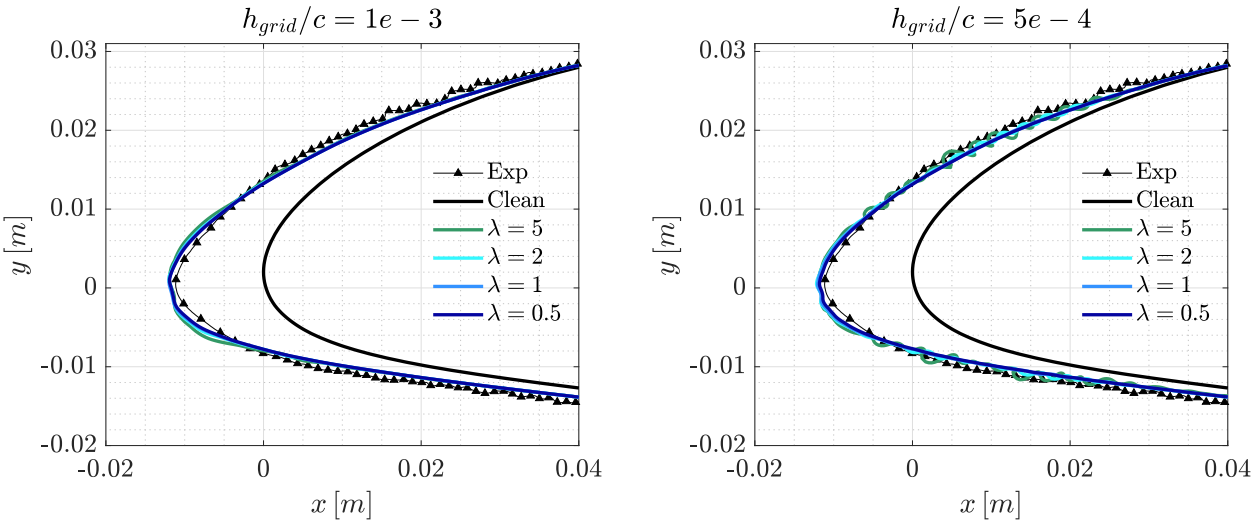


**(a) Medium grid** **(b) Fine grid**

**Fig. 3 Rime ice over a NACA 23012 airfoil. Comparison between the ice shapes computed with a medium and fine grid spacing for different values of the growth limiter $\lambda$ and the experimental data from [17].**

2, 1, and 0.5, are considered, along with two mesh sizes: the medium mesh is characterized by a boundary edge size for the discretization of the iced surface of $h_{grid}/c = 1 \cdot 10^{-3}$, while the fine mesh by $h_{grid}/c = 5 \cdot 10^{-4}$, where $c$ is the airfoil chord.

Then, the same two cases are reconsidered but simulating a real 3D straight wing to investigate the effect of the growth parameter $\lambda$ on three-dimensional ice shapes. For the 3D case, the minimum edge length for the discretization of the iced surface is set to 1mm, and three different $\lambda$ values are considered, namely 3, 2, and 1.

### A. Case 241: Rime Ice

In rime ice conditions, usually occurring at temperatures well below the freezing point, all the water freezes upon impingement, leading to the formation of relatively streamlined ice shapes. Fig. 3 shows the ice shape obtained for different values of the growth limiter $\lambda$, for each of the two spacing considered.

All the simulations overlap, regardless of the time step and the mesh size, and compare extremely well with the experimental data. However, some oscillations show up in results on the fine grid for $\lambda = 2$ and $\lambda = 5$. For the medium grid, the ice shape computed with $\lambda = 5$ is slightly less tapered than the others due to the fewer steps adopted for the simulation. These oscillations may be mistaken for valid ice evolution, leading in some circumstances to match the experimental data accurately. Instead, they result from the propagation of numerical inaccuracies. Fig. 4 and Fig.4 represent all the intermediate ice shapes of each combination of grid spacing and growth parameter, colored by the collection efficiency. For rime ice, $\beta$ is proportional to the local ice growth rate. This way, it is possible to appreciate how these oscillations do not appear immediately but progressively amplify themselves. Moreover, numerical oscillations can be observed for the medium spacing with $\lambda = 5$ in both the upper and lower surface, although characterized by a smaller amplitude. In order to trigger and amplify these oscillations, several time steps are required. This means that holding the growth parameter constant and varying the grid spacing, the larger number of time steps to get to the final

**Table 1 Test conditions: angle of attack (AoA), the freestream velocity $v_\infty$, the freestream temperature $T_\infty$, the freestream pressure $P_\infty$, the liquid water content (LWC) of the cloud, i.e. the grams of water contained in a cubic meter of air, the droplet median volume diameter (MVD) and the total icing exposure time.**

| Case | AoA [°] | $v_\infty$ [m/s] | $T_\infty$ [K] | $P_\infty$ [kPa] | LWC [g/m$^3$] | MVD [$\mu$m] | Time [s] |
|---|---|---|---|---|---|---|---|
| 241 | 2.0 | 103 | 250 | 92.528 | 0.42 | 30 | 300 |
| 242 | 2.0 | 103 | 266 | 92.941 | 0.81 | 15 | 300 |

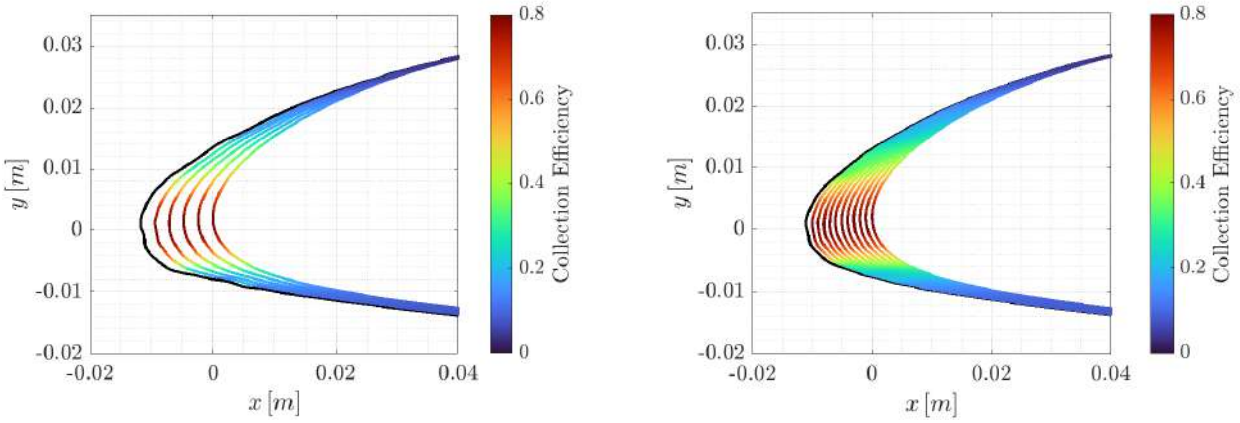


**(a) Ice shape evolution for $\lambda = 5$.** **(b) Ice shape evolution for $\lambda = 2$.**

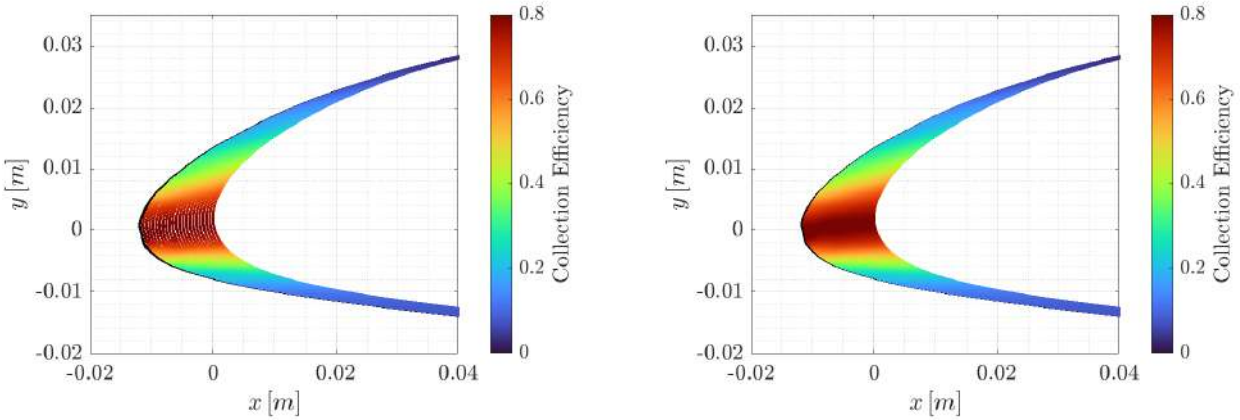


**(c) Ice shape evolution for $\lambda = 1$.** **(d) Ice shape evolution for $\lambda = 0.5$.**

**Fig. 4 Rime ice over a NACA 23012 airfoil. The evolution in time of the ice shape is colored with the local collection efficiency for different values of the growth parameter $\lambda$ over the medium grid, characterized by $h_{grid}/c = 0.001$.**

exposure time associated with the fine grid will contribute to the development of these instabilities. Another possible reason for which significant oscillations are observed for the finest grid discretization is that, during the remeshing process, larger elements tend to mitigate the appearance of these instabilities due to reduced geometrical resolution.

The considered numerical experiments suggest that selecting values of $\lambda \leq 1$ might help avoid the emergence of instabilities during multi-step simulation. This is possibly due to the amount of ice to be accreted being less or equal than the surface edge length, and/or the trajectories of the droplets are recomputed so often that any perturbation can be filled immediately. Regarding this filling effect, the more significant contribution is from the larger bins of the poly-dispersed cloud, which is discretized, according to the data provided in the IPW [17], in 7 different bins. To confirm this hypothesis, Fig. 6 represents a comparison between the ice shape evolution computed on the fine grid with $\lambda = 1$ with a multi-bin approach for the computation of the collection efficiency against its counterpart where the cloud is assumed to be monodispersed. In addition to an expected lack of ice mass near the impinging limits due to the absence of the larger and heavier droplets visible on the upper side of the airfoil, is evident also the presence of oscillations in the surface geometry on both the upper and lower side of the airfoil.

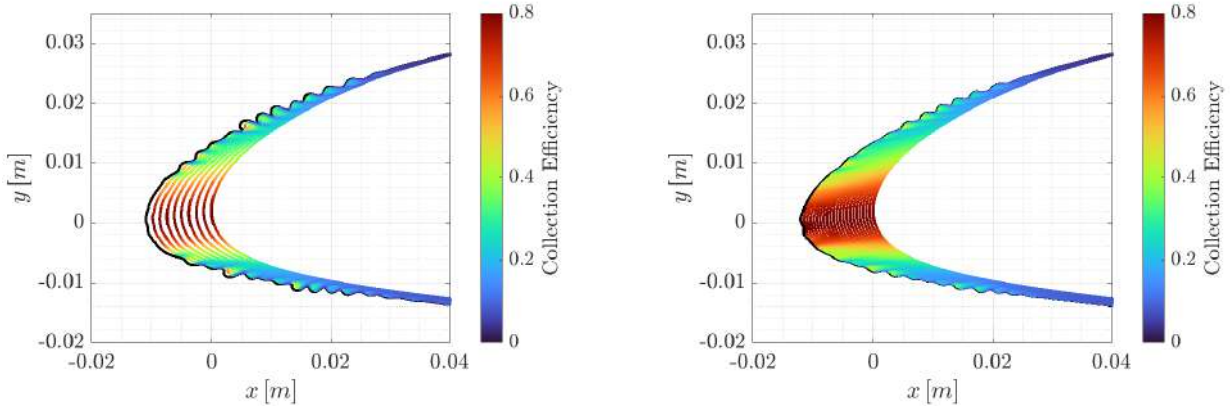


**(a) Ice shape evolution for $\lambda = 5$.** **(b) Ice shape evolution for $\lambda = 2$.**

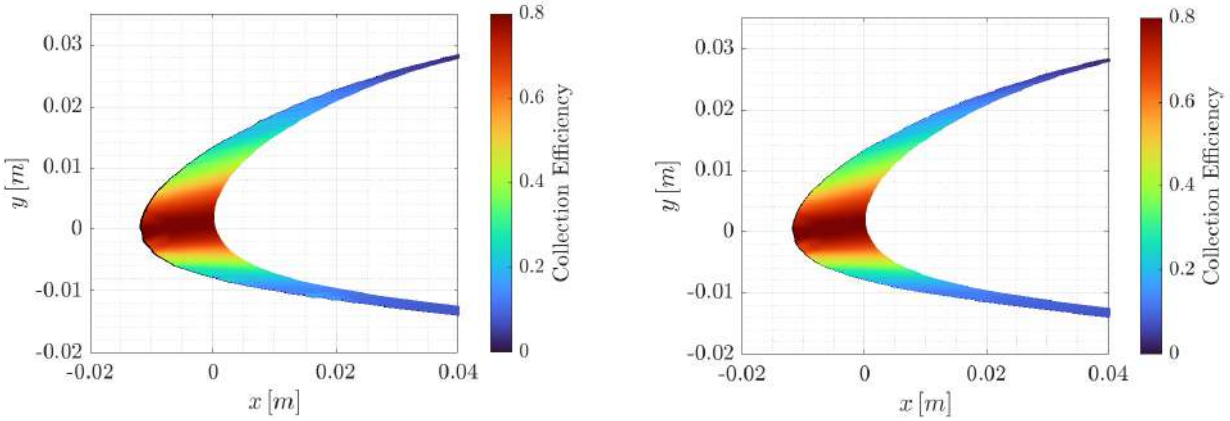


**(c) Ice shape evolution for $\lambda = 1$.** **(d) Ice shape evolution for $\lambda = 0.5$.**

**Fig. 5 Rime ice over a NACA 23012 airfoil. The evolution in time of the ice shape is colored with the local collection efficiency for different values of the growth parameter $\lambda$ over the fine grid, characterized by $h_{grid}/c = 0.0005$.**

### B. Case-242: Glaze Ice

Higher static temperature and liquid water content, and smaller MVD characterize this second test case. In particular, the relatively high temperature allows for water runback after the impinging point, leading to the formation of glaze ice, characterized by the typical double horn shape. Fig. 7 represent the ice shape obtained for different values of the growth limiter $\lambda$, for each of the two spacing considered. Differently from the previous case, the scatter of the different simulations is now much more evident. However, the ice thickness predicted at the stagnation point is the same for all the considered simulations, and it matches the experimental data very well. This result is in accordance with a previous analysis that highlighted the higher sensitivity of the horn region than that of the stagnation point [39, 40]. It is hence convenient to distinguish two kinds of convergence: the temporal one and the spatial one. Keeping the grid discretization fixed and looking at the results obtained for the different values of growth parameters, it can be seen the ice shapes obtained for $\lambda = 0.5$ and $\lambda = 1$, i.e. those associated with the larger number of time steps, are very close to each other. Looking now at these two values of $\lambda$ and changing the grid discretization, all ice shapes compare reasonably well with the experimental data, especially in terms of the position of the two ice horns, with the horns associated with the fine grid forming narrower angles than the medium grid ones. On the other hand, larger values of $\lambda$ generate completely different ice shapes, suggesting that this kind of ice regime requires a frequent update of the geometry to take into account the coupling between aerodynamics, water impingement, and the consequent runback water phenomenon, which is responsible for generating the horn-like structure.

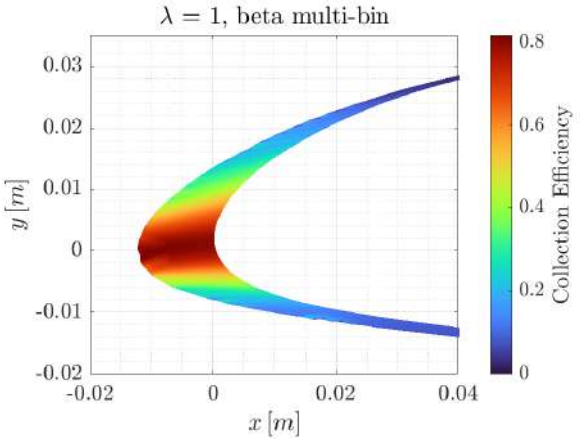


**(a) Collection efficiency computed with a 7-bins distribution.**

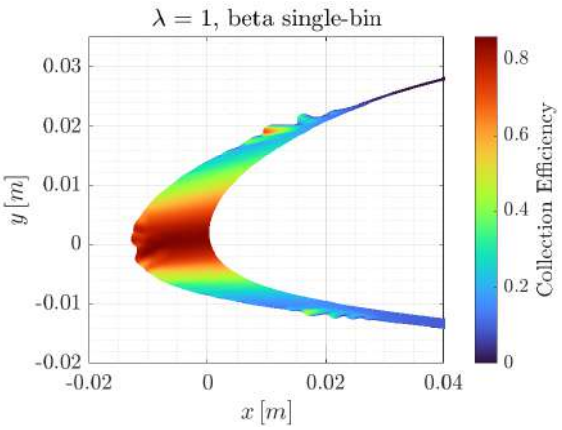


**(b) Collection efficiency computed with a single-bin distribution (MVD).**

**Fig. 6 Influence of the multi-bin distribution against the single-bin distribution when computing the collection efficiency in a multi-step simulation over the fine grid with growth parameter $\lambda$.**

Analogously to what was done for the rime ice, Fig.8 and Fig. 9 represent all the intermediate ice shapes of each combination of grid spacing and growth parameter, colored by the collection efficiency. This time, the local peaks of collection efficiency do not result in uneven ice accretion in the same spot—something that was observed for the rime ice. Indeed, given the aerodynamic heating and the relatively high temperatures on the surface, the water film flows into the adjacent cells, driven by pressure and shear stresses. No oscillations in the airfoil surface are hence formed since the runback water can fill minor surface irregularities. However, as discussed earlier, choosing an adequate time interval, or equivalently $\lambda$, is crucial to determine a consistent growth direction of the ice horns. Finally, Fig.10 represents the duration of each time-step, automatically calculated for a given growth parameter $\lambda$, for the rime case and glaze with the medium grid. While in the rime case, the duration of each time step is practically constant throughout the simulation because it depends on the maximum value of $\beta$, in the glaze case, the time step length is slightly more irregular since it depends on the mass and energy balances, influenced by the local HTC, which in turns depends on the flow solution around the changing geometry. Note that the number of time steps for e.g., $\lambda = 0.5$ is not exactly double that for $\lambda = 1$, both in the rime and the glaze case, due to the $\Delta t$ being constrained to be an integer number.

### C. Case 241: 3D Rime Ice

To investigate the effect of the growth parameter on three-dimensional ice shapes, case 241 from the $1^{st}$ Ice Prediction Workshop [17] is considered now for three different $\lambda$ values, namely 3, 2, and 1. Differently from the 2D cases, local geometrical instabilities could also lead to highly irregular ice shapes in the spanwise direction.

Fig. 11 shows the ice shape evolution at the midspan location and the comparison between the corresponding final iced geometries and the experimental results. As shown in Fig. 12, all three ice shapes almost overlap each other, proving a temporal ice-shape convergence, with slightly more tapered ice shapes as $\lambda$ is decreased, i.e., the number of time steps is increased. Differently from the 2D case, only single-bin (MVD) simulations are performed when computing the collection efficiency. This explains the lower mass deposition near the impingement limits and the slight overprediction of the total thickness at the stagnation point.

For this simple test case of icing over a straight wing, no relevant instabilities are observed even for the largest values of $\lambda$. However, as mentioned earlier, for all the 3D cases considered in this work, the minimum edge length for the ice discretization is set to 1 mm, similarly to what is usually done in the literature to compromise between accuracy and computational costs. This leads to a $h_{grid}/c$ of 0.002, which is a coarse-level mesh if compared to the mesh discretization strategy adopted for the pure 2D 241 case. This is thus coherent with what was found earlier in the 2D case, that is, the onset of geometrical instabilities requires a fine discretization and large values of $\lambda$.

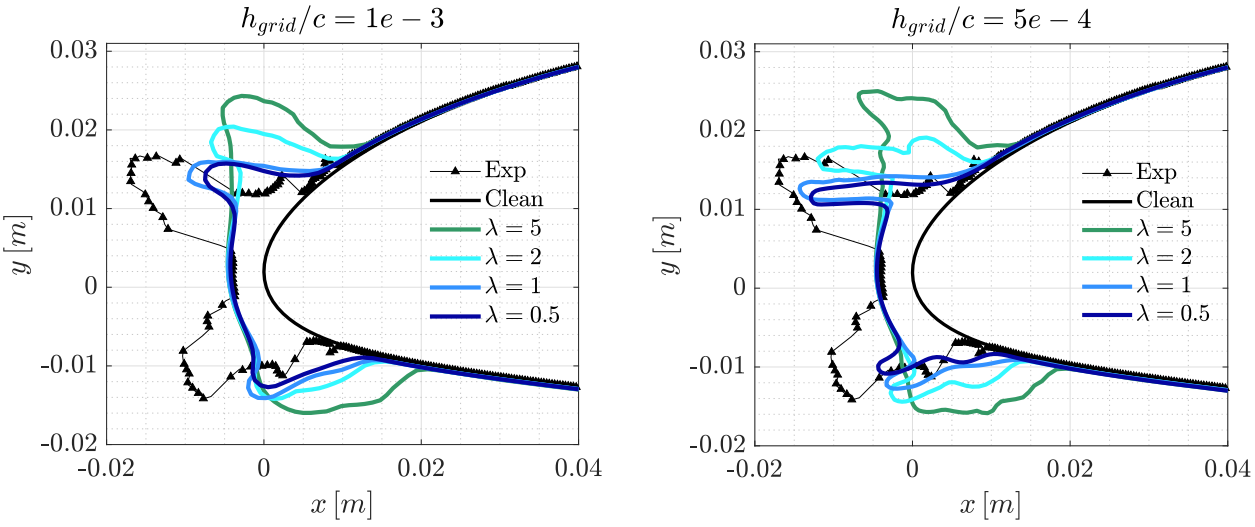


**(a) Medium grid** **(b) Fine grid**

**Fig. 7 Glaze ice over a NACA 23012 airfoil. Comparison between the ice shapes computed with a medium and fine grid spacing for different values of the growth limiter $\lambda$ and the experimental data from [17].**

### D. Case 242: 3D Glaze Ice

As previously done for case 241, case 242 is considered here as a three-dimensional straight wing. Simulations are run with three different $\lambda$ values, namely 3, 2, and 1. Differently from the rime case, the growth of geometrical instabilities does not come exclusively from local perturbations of the surface geometry, and hence of the collection efficiency, but the ice growth rate is determined by the mass and energy balance over the surface. Thus, this case aims to investigate the role of water runback and HTC distribution in the formation of irregular ice shapes, which can hinder the stability of the multi-step process.

Fig. 13 represents the ice shape evolution at the midspan location and the comparison between the corresponding final iced geometries and the experimental results. As shown in Fig. 14, the three ice shapes show a similar trend with the desired double horn behavior, characterized by slightly narrower angles as $\lambda$ is decreased. As in the 2D case, the total ice thickness at the stagnation point matches the experimental data extremely well, while the position of the horns is further back compared to the experiments. Considering that the minimum edge length for the ice discretization is set to 1 mm, and therefore $h_{grid}/c$ is around 0.002, the 3D shapes are closer to the 2D results of the medium grid rather than to the fine grid ones, as expected.

Additional investigations are required to ascertain whether this deviation from experimental results stems from an excessively coarse grid discretization of the ice shape or it may be linked to the uniform equivalent sand grain roughness employed in the CFD simulations. Indeed, the roughness value determines the calculation of heat transfer coefficients (HTC) and, consequently, influences the development of ice horns.

Differently from the rime ice case, instabilities are observed in the spanwise direction for larger values of $\lambda$. In particular, the ice shapes associated with the highest values of $\lambda$ show a wavier behavior. Moreover, the height of the upper horn is not exactly constant in the spanwise direction for each of the $\lambda$ considered. Looking at the evolution of the ice shape, it can be seen that local perturbations of the geometry are immediately reflected in the HTC computation, which determines a non-uniform ice growth rate. It should be noted that this effect is not strictly related to the choice of a uniform sand grain roughness, but the same problems are expected even for more sophisticated roughness models.

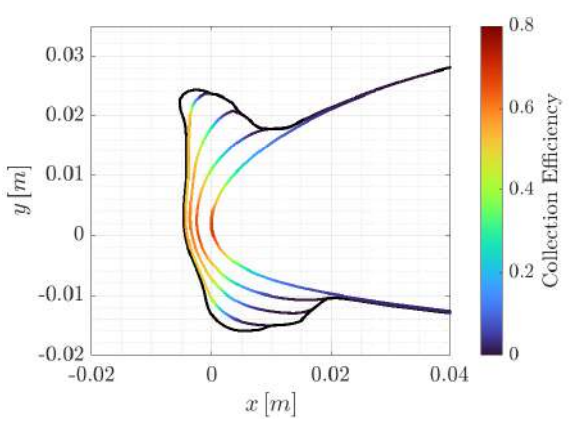


**(a) Ice shape evolution for $\lambda = 5$.**

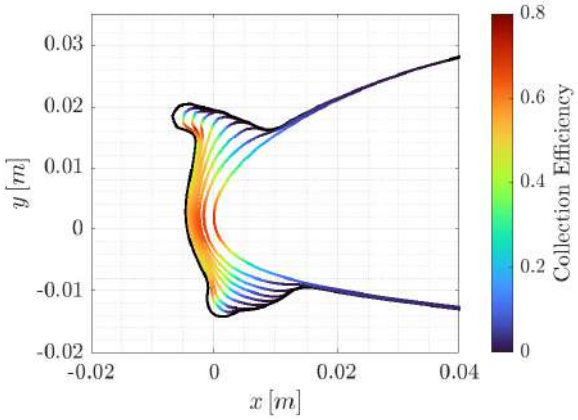


**(b) Ice shape evolution for $\lambda = 2$.**

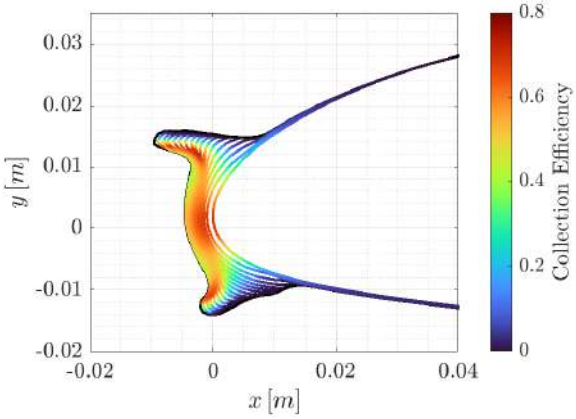


**(c) Ice shape evolution for $\lambda = 1$.**

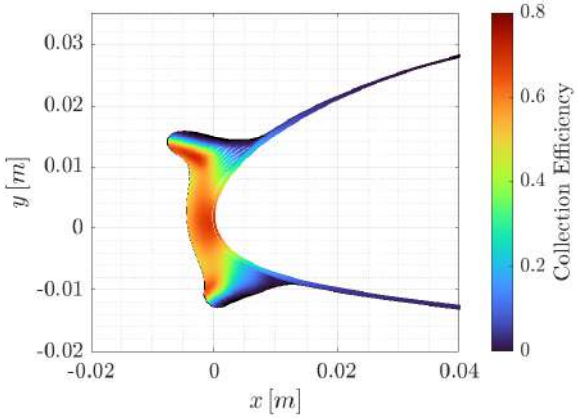


**(d) Ice shape evolution for $\lambda = 0.5$.**

**Fig. 8 Glaze ice over a NACA 23012 airfoil. The evolution in time of the ice shape is colored with the local collection efficiency for different values of the growth parameter $\lambda$ over the medium grid, characterized by $h_{grid}/c = 0.001$.**

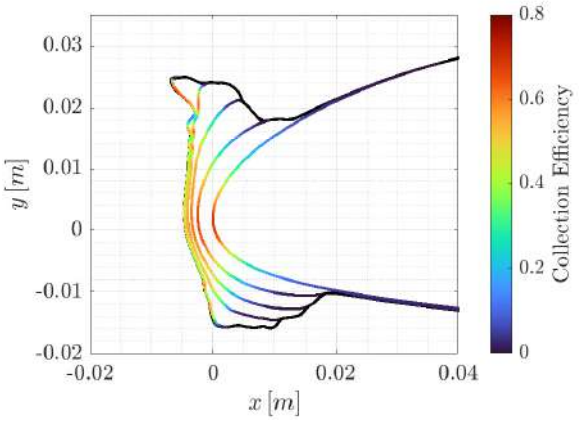


**(a) Ice shape evolution for $\lambda = 5$.**

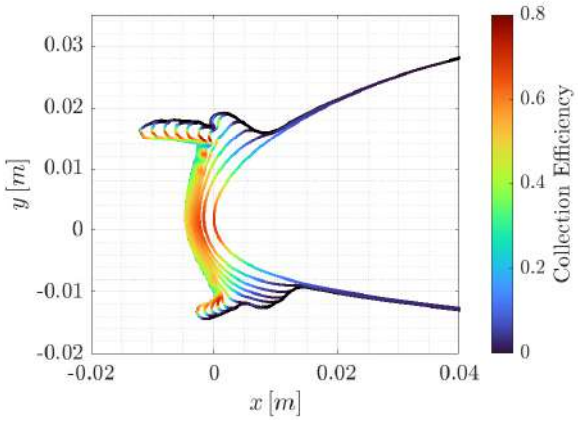


**(b) Ice shape evolution for $\lambda = 2$.**

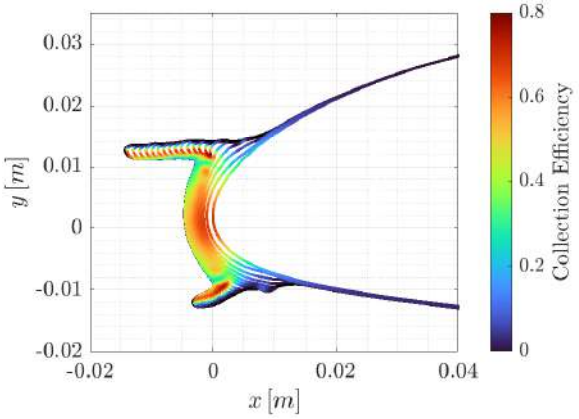


**(c) Ice shape evolution for $\lambda = 1$.**

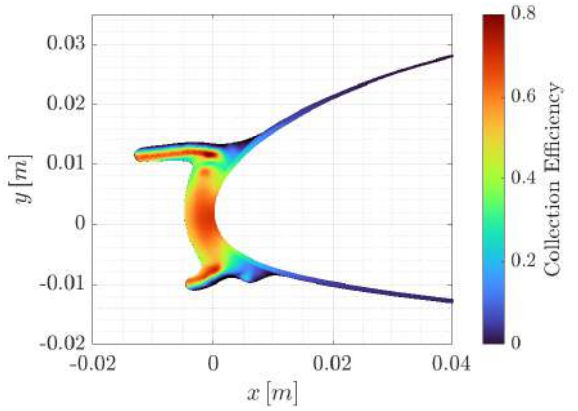


**(d) Ice shape evolution for $\lambda = 0.5$.**

**Fig. 9 Glaze ice over a NACA 23012 airfoil. The evolution in time of the ice shape is colored with the local collection efficiency for different values of the growth parameter $\lambda$ over the fine grid, characterized by $h_{grid}/c = 0.0005$.**

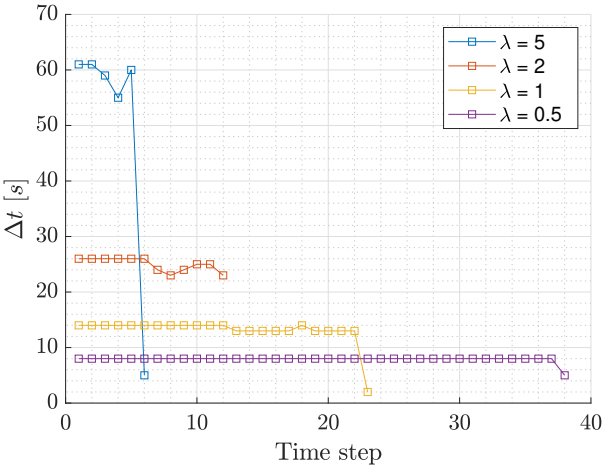


**(a) Case-241, rime ice.**

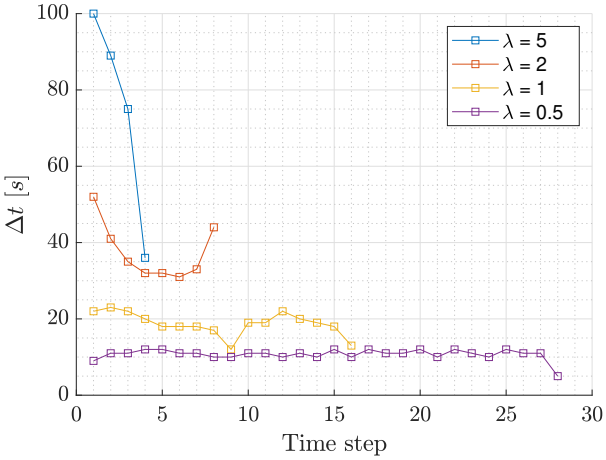


**(b) Case-242, glaze ice.**

**Fig. 10 Time steps duration at different $\lambda$ values for Case-241 and Case-242.**

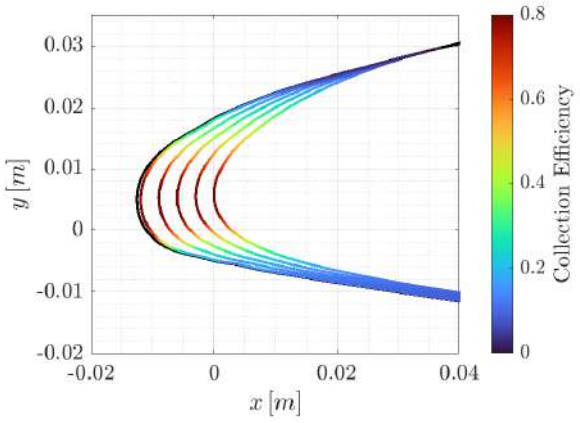


**(a) Ice shape evolution for $\lambda = 3$.**

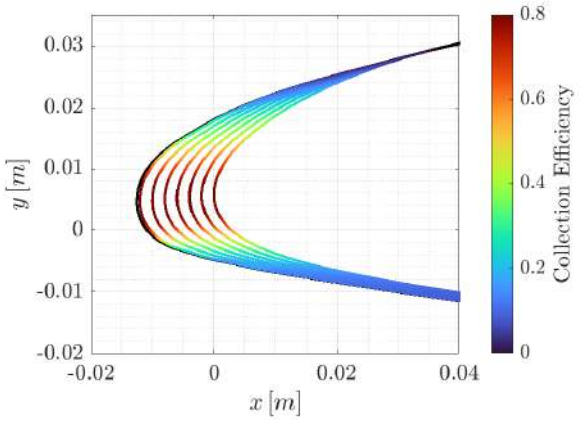


**(b) Ice shape evolution for $\lambda = 2$.**

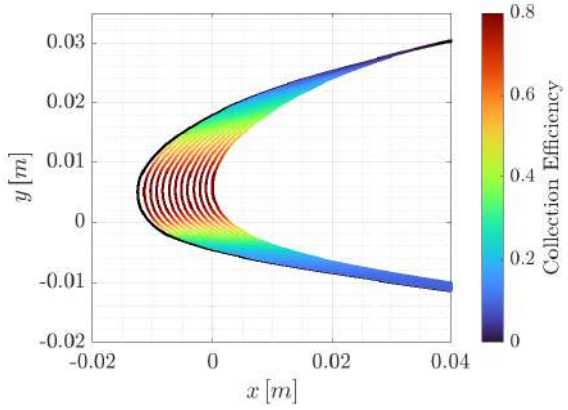


**(c) Ice shape evolution for $\lambda = 1$.**

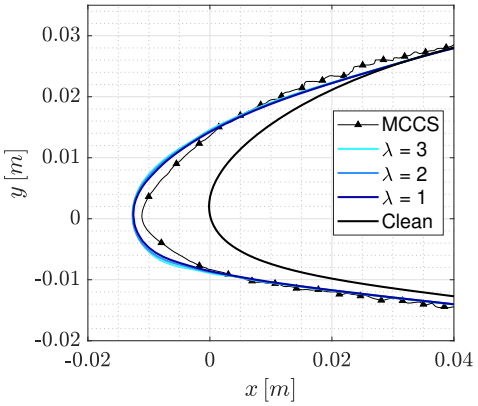


**(d) Comparison of the final ice shapes.**

**Fig. 11 Rime ice over a NACA 23012 straight wing. The evolution in time of the ice shape is colored with the local collection efficiency for different values of the growth parameter $\lambda$.**

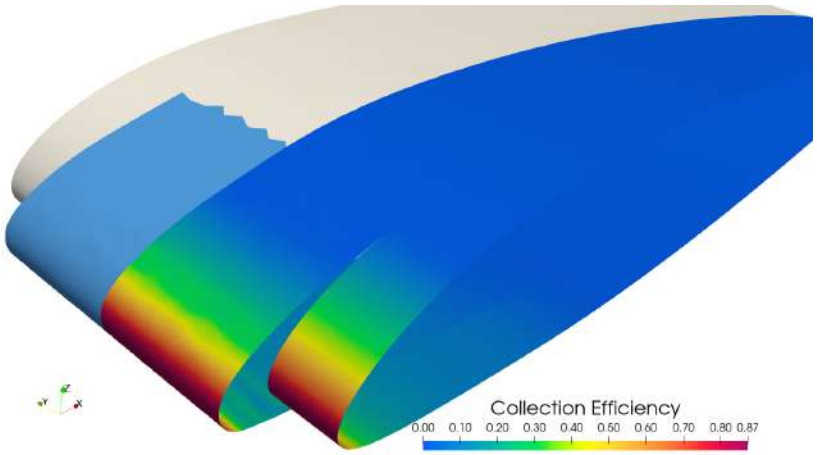


**(a) Final ice shape with $\lambda = 3$.**

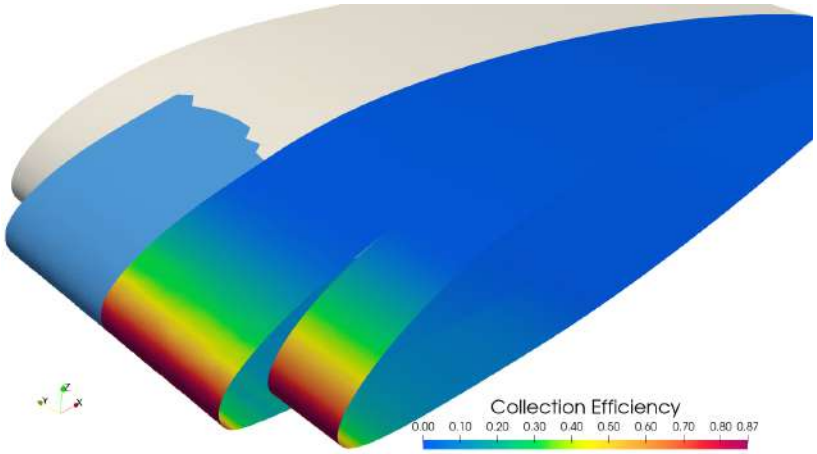


**(b) Final ice shape with $\lambda = 2$.**

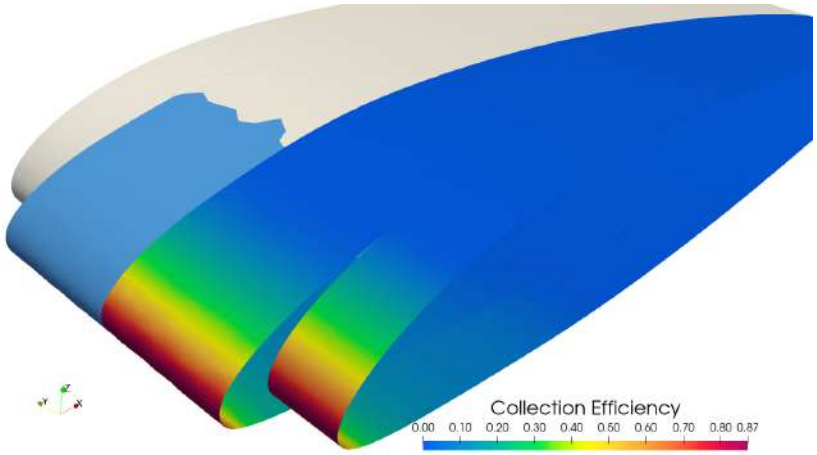


**(c) Final ice shape with $\lambda = 1$.**

**Fig. 12 Rime ice over a NACA 23012 straight wing. The left half represents the initial and final geometry, with the iced region represented in blue, while the right one shows the collection efficiency at the final and initial time.**

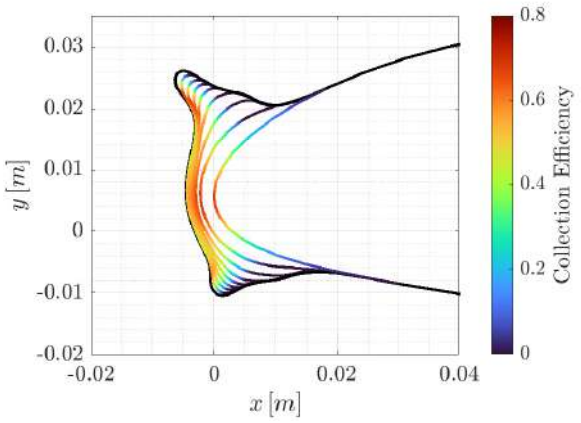


**(a) Ice shape evolution for $\lambda = 3$.**

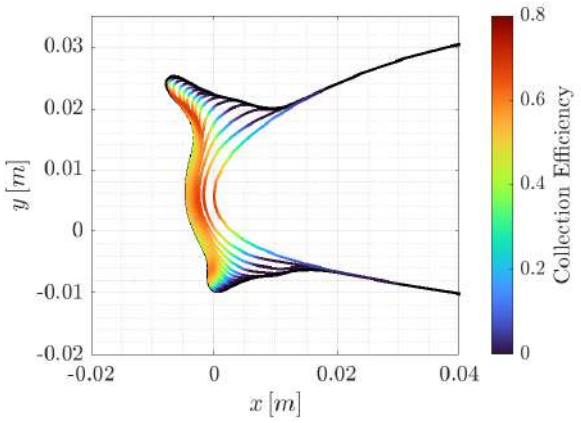


**(b) Ice shape evolution for $\lambda = 2$.**

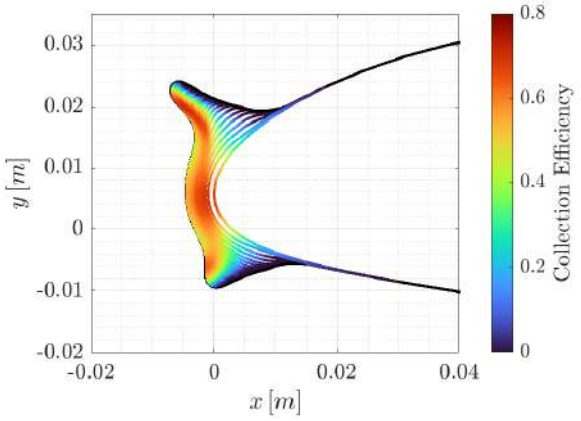


**(c) Ice shape evolution for $\lambda = 1$.**

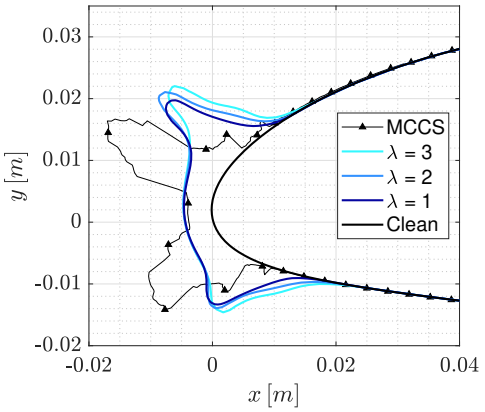


**(d) Comparison of the final ice shapes.**

**Fig. 13 Glaze ice over a NACA 23012 straight wing. The evolution in time of the ice shape is colored with the local collection efficiency for different values of the growth parameter $\lambda$.**

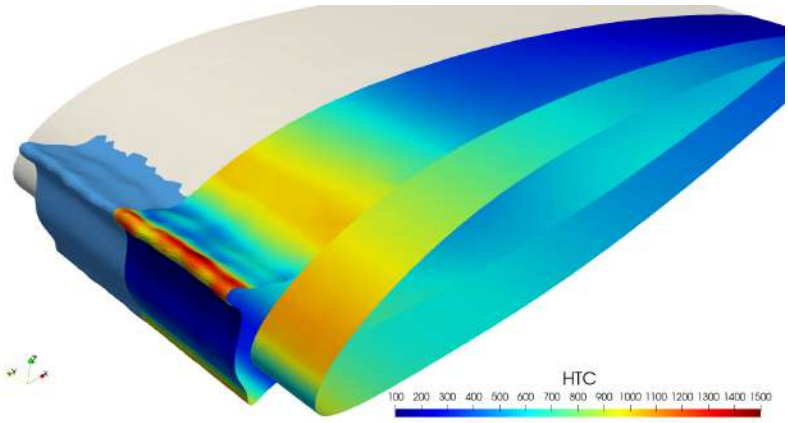


**(a) Final ice shape with $\lambda = 3$.**

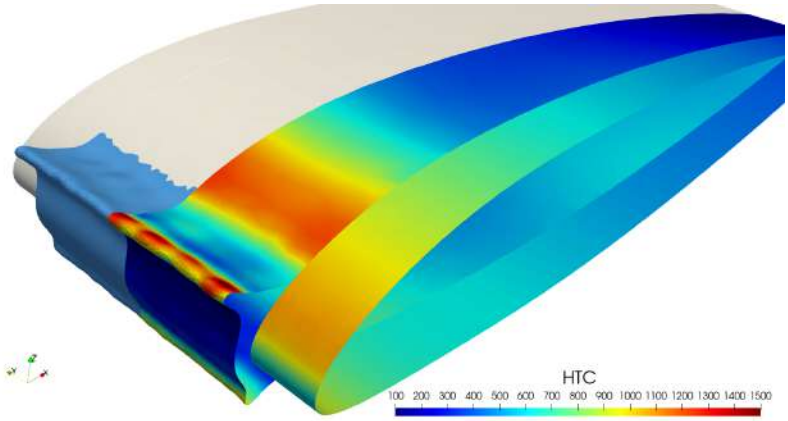


**(b) Final ice shape with $\lambda = 2$.**

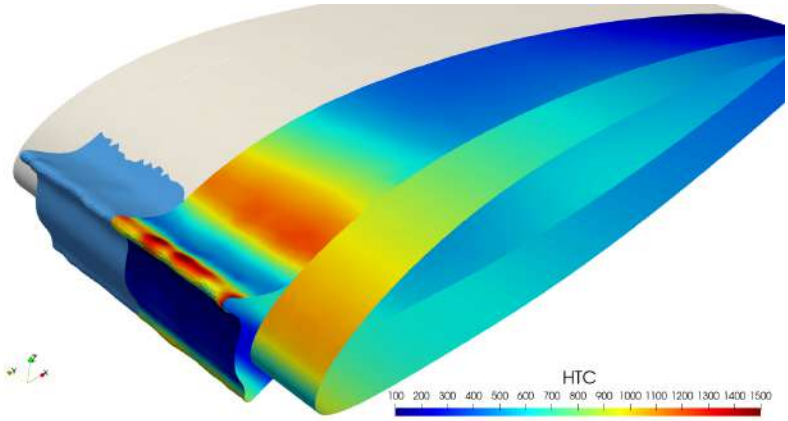


**(c) Final ice shape with $\lambda = 1$.**

**Fig. 14 Glaze ice over a NACA 23012 straight wing. The left half represents the initial and final geometry, with the iced region represented in blue, while the right one shows the HTC distribution at the final and initial time.**

## IV. Conclusions

This work presented multi-step numerical simulations of in-flight ice accretion around airfoils and wings, focusing on the effects of spatial and temporal discretization on the final ice shape. In particular, a growth parameter $\lambda$ was introduced to describe the origin and the evolution of geometrical irregularities. In this way, the duration of each intermediate step can be computed automatically within the thermodynamic module, without the need for a-priori guesses from the user. The strategy adopted for the definition of the discrete level-set field to track the updating of the evolving ice-air interface has been improved to deal with arbitrary large displacements, and its robustness has been key to complete all the simulations in an automatic way, especially those that would have lead to grid intersections if performed with standard mesh deformation techniques.

The time evolution of the ice shapes obtained for different values of $\lambda$ exposed the numerical mechanisms leading to geometrical oscillations on the iced surface, highlighting the different ice accretion mechanisms between rime ice and glaze ice and their effect on such irregularities, including the importance of multi-bin simulations to describe the physics of the process better. The grid spacing analysis clearly showed that a fine grid discretization, although capable of describing more accurately the ice features, promotes the development of geometrical oscillations if compared tothe corresponding coarser grid with the same value of growth parameter $\lambda$.

Ice shape convergence has been widely verified for the rime ice, despite the appearance of geometrical oscillations. Convergence is unfortunately more difficult to assess in the presence of large horn-like shapes as those associated with the glaze ice. Another key factor that promotes the insurgence of such oscillations is the heat transfer coefficient, which determines the local ice accretion rate. The analysis showed that very short time steps are required to have a consistent prediction of the horns' angles and that the surface discretization strongly influences their location.

Numerical simulations highlighted how a simple comparison between single slices is of limited use due to the high irregularity of the ice shape in the spanwise direction. In future investigations, other quantities such as the overall ice mass, locally computed mean ice shapes, and possibly also the time evolution of the experimental ice shape would provide valuable insights into this complex formation mechanism, helping the modeling and developing of in-flight icing simulations.

## Acknowledgments

The ICE GENESIS project has received funding from the European Union's Horizon 2020 research and innovation program under grant agreement no. 824310.

## References

[1] Wright, W., *User manual for the NASA Glenn ice accretion code LEWICE*, National Aeronautics and Space Administration, Glenn Research Center, 2002.

[2] Beaugendre, H., Morency, F., and Habashi, W. G., "FENSAP-ICE's three-dimensional in-flight ice accretion module: ICE3D," *Journal of Aircraft*, Vol. 40, No. 2, 2003, pp. 239–247. https://doi.org/10.2514/2.3113.

[3] Radenac, E., "Validation of a 3D ice accretion tool on swept wings of the SUNSET2 program," *8th AIAA Atmospheric and Space Environments Conference*, 2016, p. 3735. https://doi.org/10.2514/6.2016-3735.

[4] Petrosino, F., Mingione, G., Carozza, A., Gilardoni, T., and D'Agostini, G., "Ice accretion model on multi-element airfoil," *Journal of Aircraft*, Vol. 48, No. 6, 2011, pp. 1913–1920. https://doi.org/10.2514/1.C031346.

[5] Gori, G., Zocca, M., Garabelli, M., Guardone, A., and Quaranta, G., "PoliMIce: A simulation framework for three-dimensional ice accretion," *Applied Mathematics and Computation*, Vol. 267, 2015, pp. 96–107. https://doi.org/10.1016/j.amc.2015.05.081.

[6] Zeppetelli, D., and Habashi, W. G., "In-flight icing risk management through computational fluid dynamics-icing analysis," *Journal of aircraft*, Vol. 49, No. 2, 2012, pp. 611–621. https://doi.org/10.2514/1.C031609.

[7] Gent, R., Dart, N., and Cansdale, J., "Aircraft icing," *Philosophical Transactions of the Royal Society A: Mathematical, Physical and Engineering Sciences*, Vol. 358, No. 1776, 2000, pp. 2873–2911. https://doi.org/10.1098/rsta.2000.0689.

[8] Bourgault-Cote, S., Docampo-Sánchez, J., and Laurendeau, E., "Multi-Layer Ice Accretion Simulations Using a Level-Set Method With B-Spline Representation," *2018 AIAA Aerospace Sciences Meeting*, 2018, pp. 1–13. https://doi.org/10.2514/6.2018-1835.

[9] Caccia, F., and Guardone, A., "Numerical simulations of ice accretion on wind turbine blades: are performance losses due to ice shape or surface roughness?" *Wind Energy Science*, Vol. 8, No. 3, 2023, pp. 341–362. https://doi.org/10.5194/wes-8-341-2023.

[10] Morelli, M., Bellosta, T., and Guardone, A., "Efficient radial basis function mesh deformation methods for aircraft icing," *Journal of Computational and Applied Mathematics*, Vol. 392, 2021, p. 113492. https://doi.org/10.1016/j.cam.2021.113492.

[11] Pendenza, A., Habashi, W. G., and Fossati, M., "A 3D mesh deformation technique for irregular in-flight ice accretion," *International Journal for Numerical Methods in Fluids*, Vol. 79, No. 5, 2015, pp. 215–242. https://doi.org/10.1002/fld.4049.

[12] Ozcer, I., Switchenko, D., Baruzzi, G. S., and Chen, J., "Multi-shot icing simulations with automatic re-meshing," Tech. rep., SAE Technical Paper, 2019. https://doi.org/10.4271/2019-01-1956.

[13] Al-Kebsi, A., Mose, R., and Hoarau, Y., "Multi-Step Ice Accretion Simulation Using The Level-Set Method," *EUCASS 2019, 8th European Conference for Aeronautics and Space Sciences*, 2019, pp. 1–13. https://doi.org/10.4271/2019-01-1955.

[14] Donizetti, A., Bellosta, T., Rausa, A., Re, B., and Guardone, A., "Level-Set Mass-Conservative Front-Tracking Technique for Multistep Simulations of In-Flight Ice Accretion," *Journal of Aircraft*, 2023. https://doi.org/10.2514/1.C037027.

[15] Lavoie, P., Radenac, E., Blanchard, G., Laurendeau, E., and Villedieu, P., "Immersed Boundary Methodology for Multistep Ice Accretion Using a Level Set," *Journal of Aircraft*, 2022, pp. 1–15. https://doi.org/10.2514/1.C036492.

[16] Donato de Rosa, D. C., Francesco Capizzano, "Multi-Step Ice Accretion by Immersed Boundaries," Tech. rep., SAE Technical Paper, 2023. https://doi.org/10.4271/2023-01-1484.

[17] Laurendeau, E., Bourgault-Cote, S., Ozcer, I. A., Hann, R., Radenac, E., and Pueyo, A., "Summary from the 1st AIAA Ice Prediction Workshop," *AIAA AVIATION 2022 Forum*, 2022. https://doi.org/10.2514/6.2022-3398.

[18] Economon, T. D., and Palacios, F., and Copeland, S. R., and Lukaczyk, T. W., and Alonso, J. J., "SU2: An Open-Source Suite for Multiphysics Simulation and Design," *AIAA Journal*, Vol. 54, No. 3, 2015, pp. 828–846. https://doi.org/10.2514/1.J053813.

[19] Roe, P., "Approximate Riemann solvers, parameter vectors, and difference schemes," *Journal of Computational Physics*, Vol. 43, No. 2, 1981, pp. 357–372. https://doi.org/10.1016/0021-9991(81)90128-5.

[20] Spalart, P., and Allmaras, S., "A One-Equation Turbulence Model for Aerodynamic Flows," *AIAA*, Vol. 439, 1992. https://doi.org/10.2514/6.1992-439.

[21] Gomes, P., Economon, T. D., and Palacios, R., "Sustainable High-Performance Optimizations in SU2," *AIAA Scitech 2021 Forum*, 2021. https://doi.org/10.2514/6.2021-0855.

[22] Bellosta, T., Baldan, G., Sirianni, G., and Guardone, A., "Lagrangian and Eulerian algorithms for water droplets in in-flight ice accretion," *Journal of Computational and Applied Mathematics*, Vol. 429, 2023, p. 115230. https://doi.org/10.1016/j.cam.2023.115230.

[23] Baldan, G., Bellosta, T., and Guardone, A., "Efficient Lagrangian particle tracking algorithms for distributed-memory architectures," *Computers & Fluids*, Vol. 256, 2023, p. 105856. https://doi.org/10.1016/j.compfluid.2023.105856.

[24] Morelli, M., Bellosta, T., Donizetti, A., and Guardone, A., "Assessment of the PoliMIce toolkit from the 1st AIAA Ice Prediction Workshop," *AIAA AVIATION 2022 Forum*, 2022. https://doi.org/10.2514/6.2022-3307.

[25] Stefan, J., "Ueber die Theorie der Eisbildung, insbesondere über die Eisbildung im Polarmeere," *Annalen der Physik*, Vol. 278, No. 2, 1891, pp. 269–286. https://doi.org/10.1002/andp.18912780206.

[26] Messinger, B., "Equilibrium Temperature of an Unheated Icing Surface as a Function of Air Speed," *Journal of the Aeronautical Sciences*, Vol. 20, 1953, pp. 29–42. https://doi.org/10.2514/8.2520.

[27] Zhu, C., Fu, B., Sun, Z., and Zhu, C., "3D ICE ACCRETION SIMULATION FOR COMPLEX CONFIGURATION BASING ON IMPROVED MESSINGER MODEL," *International Journal of Modern Physics: Conference Series*, Vol. 45, 2012, pp. 341–350. https://doi.org/10.1142/S2010194512008938.

[28] Bourgault, Y., Beaugendre, H., and Habashi, W. G., "Development of a Shallow-Water Icing Model in FENSAP-ICE," *Journal of Aircraft*, Vol. 37, No. 4, 2000, pp. 640–646. https://doi.org/10.2514/2.2646.

[29] Myers, T., "Extension to the Messinger model for aircraft icing," *AIAA Journal*, Vol. 39, 2001, pp. 211–218. https://doi.org/10.2514/2.1312.

[30] Gori, G., Parma, G., Zocca, M., and Guardone, A., "Local Solution to the Unsteady Stefan Problem for In-Flight Ice Accretion Modeling," *Journal of Aircraft*, Vol. 55, No. 1, 2018, pp. 251–262. https://doi.org/10.2514/1.C034412.

[31] Shin, J., Berkowitz, B., Chen, H., and Cebeci, T., "Prediction of ice shapes and their effect on airfoil performance," *29th Aerospace Sciences Meeting*, 1991, p. 264. https://doi.org/10.2514/6.1991-264.

[32] Ravishankara, A., Bakhmet, I., and Özdemir, H., "Estimation of roughness effects on wind turbine blades with vortex generators," *Journal of physics: Conference series*, Vol. 1618, 2020, p. 052031. https://doi.org/10.1088/1742-6596/1618/5/052031.

[33] Osher, S., and Fedkiw, R., *Level set methods and dynamic implicit surfaces*, Springer Science & Business Media, 2006.

[34] Arya, S., Mount, D. M., Netanyahu, N. S., Silverman, R., and Wu, A. Y., "An optimal algorithm for approximate nearest neighbor searching fixed dimensions," *Journal of the ACM (JACM)*, Vol. 45, No. 6, 1998, pp. 891–923. https://doi.org/10.1145/293347.293348.

[35] Dapogny, C., Dobrzynski, C., and Frey, P., "Three-dimensional adaptive domain remeshing, implicit domain meshing, and applications to free and moving boundary problems," *Journal of Computational Physics*, Vol. 262, 2014, pp. 358–378. https://doi.org/10.1016/j.jcp.2014.01.005.

[36] Rausa, A., Donizetti, A., and Guardone, A., "Multi-physics simulation of 3D in-flight ice-shedding," *Journal of Computational and Applied Mathematics*, Vol. 432, 2023, p. 115226. https://doi.org/10.1016/j.cam.2023.115226.

[37] Fidelity Pointwise for CFD Meshing, https://www.cadence.com/en_US/home/tools/system-analysis/computational-fluid-dynamics/pointwise.html, 2007.

[38] Donizetti, A., Rausa, A., Bellosta, T., Re, B., and Guardone, A., "A Three-Dimensional Level-Set Front Tracking Technique for Automatic Multi-Step Simulations of In-Flight Ice Accretion," Tech. rep., SAE Technical Paper, 2023. https://doi.org/10.4271/2023-01-1467.

[39] Gori, G., Congedo, P. M., Le Maître, O., Bellosta, T., and Guardone, A., "Modeling In-Flight Ice Accretion Under Uncertain Conditions," *Journal of Aircraft*, Vol. 59, No. 3, 2022, pp. 799–813. https://doi.org/10.2514/1.C036545.

[40] Bellosta, T., Guardone, A., Gori, G., Congedo, P., and Le Maître, O., "Uncertainty quantification for in-flight ice accretion under Appendix-C and Appendix-O conditions," *AIAA AVIATION FORUM*, 2021. https://doi.org/10.2514/6.2021-2645.